AGU PUBLICATIONS

Geophysical Research Letters

RESEARCH LETTER
10.1002/2015GL065169

Special Section:
First Results from the MAVEN Mission to Mars

Model insights into energetic photoelectrons measured at Mars by MAVEN

Shotaro Sakai[1], Ali Rahmati[1], David L. Mitchell[2], Thomas E. Cravens[1], Stephen W. Bougher[3], Christian Mazelle[4,5], W. K. Peterson[6], Francis G. Eparvier[6], Juan M. Fontenla[7], and Bruce M. Jakosky[6]

[1]Department of Physics and Astronomy, University of Kansas, Lawrence, Kansas, USA, [2]Space Science Laboratory, University of California, Berkeley, California, USA, [3]Department of Atmospheric, Oceanic and Space Sciences, University of Michigan, Ann Arbor, Michigan, USA, [4]IRAP, UPS-OMP, Université de Toulouse, Toulouse, France, [5]IRAP, CNRS, Toulouse, France, [6]Laboratory for Atmospheric and Space Physics, University of Colorado Boulder, Boulder, Colorado, USA, [7]NorthWest Research Associates, Redmond, Washington, USA

Key Points:
- Photoelectrons are diagnostic of solar energy deposited in atmosphere of Mars
- Low-energy photoelectron fluxes depend on the ionospheric electron density
- Precipitation of external electrons contributes to measured electron fluxes

Correspondence to:
T. E. Cravens,
cravens@ku.edu

Citation:
Sakai, S., A. Rahmati, D. L. Mitchell, T. E. Cravens, S. W. Bougher, C. Mazelle, W. K. Peterson, F. G. Eparvier, J. M. Fontenla, and B. M. Jakosky (2015), Model insights into energetic photoelectrons measured at Mars by MAVEN, *Geophys. Res. Lett.*, *42*, 8894–8900, doi:10.1002/2015GL065169.

Received 30 JUN 2015
Accepted 8 AUG 2015
Published online 5 NOV 2015
Corrected 3 FEB 2016

This article was corrected on 3 FEB 2016. See the end of the full text for details.

Abstract Photoelectrons are important for heating, ionization, and airglow production in planetary atmospheres. Measured electron fluxes provide insight into the sources and sinks of energy in the Martian upper atmosphere. The Solar Wind Electron Analyzer instrument on board the MAVEN (Mars Atmosphere and Volatile EvolutioN) spacecraft measured photoelectrons including Auger electrons with 500 eV energies. A two-stream electron transport code was used to interpret the observations, including Auger electrons associated with *K* shell ionization of carbon, oxygen, and nitrogen. It explains the processes that control the photoelectron spectrum, such as the solar irradiance at different wavelengths, external electron fluxes from the Martian magnetosheath or tail, and the structure of the upper atmosphere (e.g., the thermal electron density). Our understanding of the complex processes related to the conversion of solar irradiances to thermal energy in the Martian ionosphere will be advanced by model comparisons with measurements of suprathermal electrons by MAVEN.

1. Introduction

Solar extreme ultraviolet (EUV) and soft X-ray radiation deposit energy in the Martian upper atmosphere [cf. *Fox et al.*, 2008]. Photoelectrons (or suprathermal electrons) result from the photoionization of neutral species (CO_2, CO, N_2, and O):

$$h\nu + CO_2 \rightarrow CO_2^+ + e^- \quad (1)$$

The energy of a photoelectron (E) is the photon energy ($h\nu$, where h is Planck's constant and ν is the photon frequency) minus the ionization potential (I_{nj}) of relevant neutral species (n) and ion final state (j): $E = h\nu - I_{nj}$. Solar extreme ultraviolet (EUV) photons produce electrons with E less than ≈ 100 eV, and soft X-rays produce higher energy electrons. Photoelectrons were first measured in the Martian ionosphere by the Viking Retarding Potential Analyzer [*Mantas and Hanson*, 1979]. The magnetotail can also act as a source of suprathermal electrons for the ionosphere if the magnetic topology is favorable [*Liemohn et al.*, 2006]. Ions and electrons from the solar wind that make it past the magnetic pileup region can also deposit energy in the upper atmosphere [*Crider et al.*, 2004]. Crustal magnetic fields affect the distribution of photoelectrons [*Liemohn et al.*, 2006], but the current paper will not consider this case.

Photoelectrons, and suprathermal electrons in general, have also been measured in the upper atmospheres of other planets and satellites including the Earth, Venus, Titan, Enceladus, and comets [e.g., *Lee et al.*, 1980; *Coates et al.*, 2008, 2011; *Richard et al.*, 2011; *Ozak et al.*, 2012]. At all these bodies, photoelectrons are an important indicator of solar energy input into the upper atmosphere and have also provided information on the magnetic topology.

One particularly interesting feature sometimes observed in photoelectron spectra is a flux peak due to Auger electrons, which are produced by photoionization from the *K* shell of an atom (often contained in a molecule). The first, and the only until MAVEN arrived, detection of Auger electrons at Mars was by the electron reflectometer experiment on board the Mars Global Surveyor [*Mitchell et al.*, 2000]. The ACIS-I

Table 1. Mars Solar Irradiance for Three Energy Ranges From the HESSR Solar Irradiance Model on Each Date[a]

Wavelength	2015/04/01	2015/03/03	2014/10/15	2014/10/19
0–5 nm	0.196	0.195	0.337	0.308
5–30 nm	1.16	1.18	1.60	1.53
30–100 nm	2.36	1.77	2.67	2.56

[a]The units are mW/m^2. Dates are formatted as year/month/day.

(Advanced CCD Imaging Spectrometer) instrument on board the Chandra X-ray Observatory found soft X-ray luminosities of several MW (megawatts) on the disk of Mars in addition to a faint X-ray halo by solar wind interaction with the exosphere [*Dennerl*, 2002]. The disk emission was attributed to the Auger X-rays by solar fluorescence and ionization from *K* shells of atoms contained in CO_2 [*Dennerl*, 2002; *Cravens and Maurellis*, 2001]. However, *K* shell ionization almost always (99%) produces Auger electrons as explained in section 3.

The instruments on board the MAVEN (Mars Atmosphere and Volatile EvolutioN) spacecraft started to observe the upper atmosphere and ionosphere in October 2014 with the goal of determining escape rates of volatile species. The Solar Wind Electron Analyzer (SWEA) instrument on board MAVEN has measured photoelectrons, including Auger electrons, in the upper atmosphere. In the current paper we compare measured fluxes with fluxes from our electron model to interpret different parts of the electron energy spectrum.

2. Model Description

The model has two major components: (1) a photon energy deposition code (photon code) and (2) a two-stream electron transport code (two-stream code). The photon code generates the initial production rate of suprathermal electrons as a function of altitude and energy. The two-stream code then determines electron fluxes, thermal electron heating rates, and electron impact ionization rates, although only the electron fluxes will be discussed in the current paper.

2.1. Primary Photoelectron Production Rates

The photon code requires inputs of solar spectrum irradiance, ionospheric neutral and electron densities, and absorption and photoionization cross sections. We used the Heliospheric Environment Solar Spectrum Radiation (HESSR) model, based on the Solar Irradiance Physical Modeling (SRPM) system, for the solar irradiance [e.g., *Fontenla et al*., 2011]. HESSR solar irradiance is computed from the radiance of a set of features inferred on the solar disk viewed from Mars. These features are determined from observations made at Earth using daily single-snapshot images from the Solar Dynamics Observatory near 0:00 UT and are not intended to include flares. We adopted a wavelength (λ) bin size of 0.05 nm for λ less than 6.0 nm and a size of 1.0 nm for λ greater than 6.0 nm. Solar irradiances at Mars for different wavelength intervals from HESSR are listed in Table 1 and will be discussed later. The Earth-Sun-Mars angle was 80–90° on 15 and 19 October 2014, about 150° on 3 March 2015, and about 135° on 1 April 2015.

The photoelectron production rate is calculated based on methods described by *Schunk and Nagy* [2009]. Absorption and ionization cross sections for CO_2, CO, N_2, and O are used to determine the production rate of suprathermal electrons and are taken from *Gan et al*. [1990]. As an example, the total photoionization cross section for CO_2 is shown in Figure 1a. The peaks below 50 nm are associated with ionization from the *K* shells of C and O and will be discussed later. *K* shell cross sections were also discussed by *Cravens and Maurellis* [2001].

The neutral (CO_2, CO, N_2, and O) and electron densities were taken from a dayside radial cut at a solar zenith angle of 60° from the University of Michigan's MTGCM (Mars Thermospheric General Circulation Model) for solar cycle maximum [*Bougher*, 2012; *Bougher et al*., 2009, 2014], and they are shown in Figure 1b. The neutral densities from the MTGCM model appear to be within a factor of 2 of those from the Neutral Gas and Ion Mass Spectrometer (NGIMS) on board MAVEN [*Mahaffy et al*., 2015]. Electron densities vary with solar zenith angle, particularly near the terminator, and with solar conditions, but the MTGCM values we used should be representative, as we wait for MAVEN data.

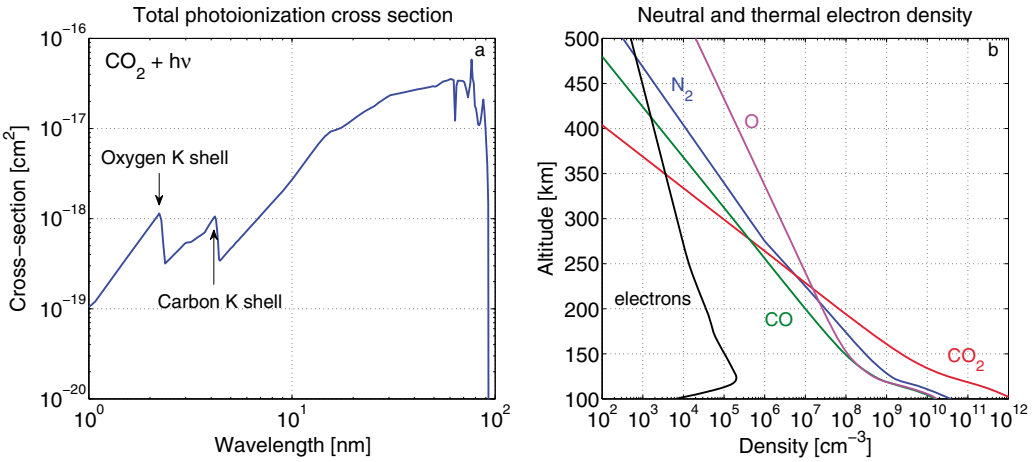

Figure 1. (a) Total photoionization cross section of CO_2. (b) Background neutral and thermal electron densities in the Martian upper atmosphere. The CO_2 (red), CO (green), N_2 (blue), O (magenta), and thermal electrons (black) are included in this model.

2.2. Suprathermal Electron Transport Equations

The two-stream code we used to calculate electron fluxes in the Martian ionosphere was originally developed for the Earth by *Nagy and Banks* [1970] and *Banks and Nagy* [1970] and adapted by many researchers for many planets. *Gan et al.* [1990, 1992] used this method to find electron fluxes along magnetic field lines near comet Halley, Venus, and Titan. The model determines electron fluxes versus distance s along the field (s is a function of altitude between 100 km and 500 km) and versus energy, ε, between 0.5 eV and 10 keV. Pitch angles in the two-stream model are either up (up flux Φ^+) or down (Φ^-) the magnetic field [e.g., *Richard et al.*, 2011; *Ozak et al.*, 2012]. The equations solved are

$$\langle\mu\rangle\frac{d\Phi^{\pm}}{ds} = -\sum_k n_k(s)\left(\sigma_a^k + p_s^k\sigma_s^k\right)\Phi^{\pm}(\varepsilon,s) + \sum_k n_k(s)p_e^k\sigma_e^k\Phi^{\mp}(\varepsilon,s) + \frac{q(\varepsilon,s)}{2} + q^{\pm}(\varepsilon,s) \quad (2)$$

where μ is cos α, α is the pitch angle, ${\sigma_a}^k$ are total inelastic collision cross sections for neutral species k, ${p_s}^k$ are backscatter probabilities. Elastic collision probabilities and cross sections are ${p_e}^k$ and ${\sigma_e}^k$, respectively. The primary production rate in the range ε to $\varepsilon + d\varepsilon$ due to photoionization by solar radiation is denoted $q(\varepsilon,s)$, and $q^{\pm}$ are cascading production rates in the range ε to $\varepsilon + d\varepsilon$ due to inelastic collisions from higher energy electrons [*Nagy and Banks*, 1970]. Each inelastic process included has an energy loss (i.e., threshold energy). For ionization, this energy includes the ionization potential as well as the secondary electron energy. The electrons lost at a given energy reappear at various lower energies (i.e., the original energy minus the energy loss of a process) with a probability proportional to the cross section for that process. This is taken into account in the cascading production rate in the equations. We assume that the average of cos $\alpha = 0.5$ (i.e., hemispherically isotropic upward and downward distributions). Electron elastic and inelastic impact cross sections are taken from *Gan et al.* [1990, and references therein].

Electron-electron Coulomb collisions compete with electron-CO_2 inelastic collisions (mainly vibrational excitation) for energies below about 10 eV. How this affects the electron flux depends on the electron-neutral density ratio in the thermosphere. The ratio of energy loss rates for Coulomb to CO_2 inelastic collisions is approximately 10^4 (n_e/n_n), where n_e and n_n are the electron and CO_2 densities, respectively. This ratio is about unity at an altitude of 200 km (densities taken from Figure 1). The thermal electrons gain energy from the Coulomb process [cf. *Schunk and Nagy*, 2009].

A draped magnetic field (parabolic) topology was adopted, and the field dip angle depends on the altitude but is overall less than several degrees. The radius of curvature at the apex point (100 km), where the parabola intersects the line of symmetry and is closest to the center of Mars, is the distance from the apex point to the center of Mars. This configuration gives a parabola with monotonically increasing radial distances with increasing angle from the apex [e.g., *Richard et al.*, 2011]. The model results are not sensitive to the details of the magnetic topology. Magnetic field measurements for the cases (and locations) chosen did not indicate the presence of crustal fields.

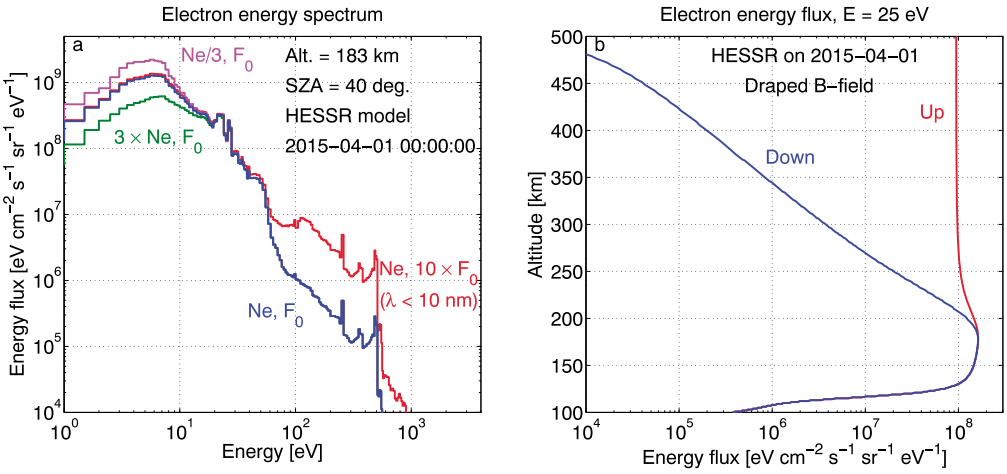

Figure 2. Energy fluxes of electrons going up and down, and at a solar zenith angle of 40°. The magnetic field dip angle depends on the altitude in our model but is overall less than several degrees (i.e., draped magnetic field). The HESSR solar irradiance model for 1 April 2015 was used. (a) Energy spectrum of omnidirectional electron flux (average of up and down fluxes) at an altitude of 183 km. The subcases with increased solar flux (red for $\lambda < 10$ nm), F_0, and altered electron densities (pink for low density and green for high density), N_e, are also displayed. The electron fluxes have a peak around 25 eV due to the ionization by solar EUV, as well as peaks above 200 eV due to Auger electrons by solar soft X-rays. (b) Upward (red) and downward (blue) energy fluxes as a function of altitude for an energy of 25 eV on the same date as for Figure 2a.

2.3. Case Studies for This Paper

Three cases were considered: (1) no-flare conditions (3 March and 1 April 2015) for which appropriate HESSR irradiances were adopted, (2) enhanced magnetosheath (or tail) electrons (15 October 2014), and (3) flare and a coronal mass ejection (CME) (19 October 2014). The HESSR solar irradiances for these dates were used in our simulations. Table 1 lists integrated solar irradiances for three wavelength intervals from HESSR (in lieu of showing the whole spectrum). As mentioned earlier, the *Bougher et al.* [2009, 2014] MTGCM densities were adopted.

Several versions of case 1 were run to test what affects the fluxes. The low-wavelength (for $\lambda < 10$ nm) solar irradiance was increased by a factor of 10, and the thermal ionospheric electron density was increased and decreased by a factor of 3 from the MTGCM model values (Figure 2a).

For cases 1 and 3 no external electrons were included (i.e., zero down flux upper boundary condition on the equations). For case 3 the HESSR daily irradiance does not include flares, but the MAVEN EUVM instrument detected a tenfold increase in the soft X-ray irradiance (but not at other wavelengths), so we boosted our solar irradiances by this factor for λ less than 5.0 nm. Note that no enhanced electrons by a CME were included. For case 2 we adopted a Maxwellian electron distribution (assumed to originate in the magnetotail) with a density of 0.5 cm^{-3} and a temperature of 50 eV for the top boundary input flux [e.g., *Shutte et al.*, 1989].

3. Auger Electrons

The ions produced by photoionization from the *K* shells of carbon, nitrogen, or oxygen atoms (contained mainly in CO_2 and N_2 molecules) are electronically excited [cf. *Fox et al.*, 2008] and can deexcite in two ways: (1) emission of an "Auger" electron or (2) emission of an X-ray photon. For oxygen these reactions can be represented by

$$O + h\nu \rightarrow O^{+*} + e^- \tag{3}$$

$$O^{+*} \rightarrow O^{++} + e^- (\approx 0.999 \text{ branching ratio, Auger electrons}) \tag{4}$$

$$\rightarrow O^+ + h\nu (\approx 0.001 \text{ branching ratio, X-rays}). \tag{5}$$

X-rays from the latter process were observed from Mars by the Chandra X-Ray Observatory [*Dennerl*, 2002; *Cravens and Maurellis*, 2001]. Figure 1a shows the CO_2 photoionization cross section with its *K* shell "edges" at 2.2 nm and 4.4 nm. The energy of Auger electrons is different according to species. The energy of carbon

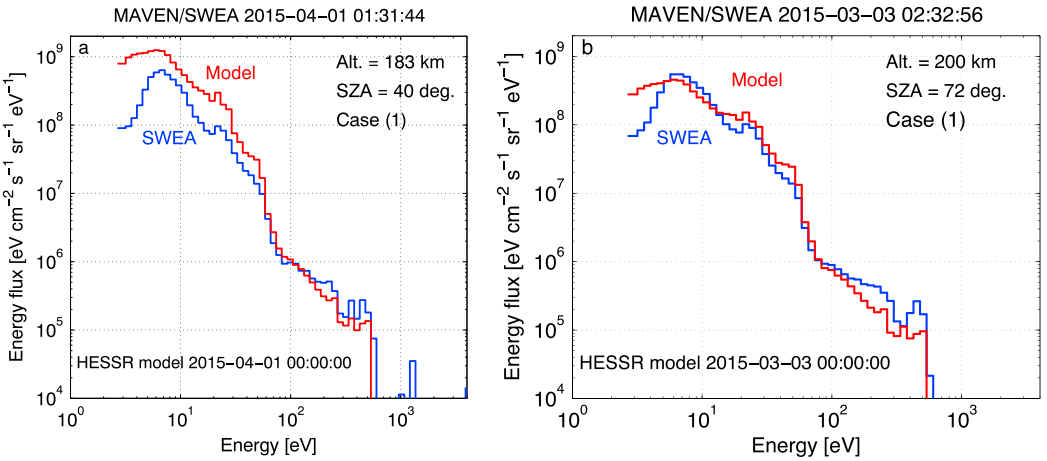

Figure 3. Two-stream model (red) and SWEA (blue) energy flux spectra for (a) 1 April 2015 and (b) 3 March 2015. The model fluxes were rebinned to match the SWEA energy resolution.

Auger electrons is ≈ 280 eV (or 4.4 nm) and of nitrogen Auger electrons is ≈ 360 eV (or 3.4 nm). More specifically, oxygen Auger electrons from CO_2 are known to have 3 closely spaced peaks at 490, 495, and 500 eV [e.g., *Víkor et al*., 1998], and we include these peaks in our model. The energies of Auger electrons are calculated based on the binding energies of *K* shell electrons for every atomic species in the photon code. The production due to ionization from the *K* shell is divided equally among the three peaks discussed and included in $q^{\pm}$ of equation (2).

4. Results

Case 1. Figure 2a shows energy fluxes at an altitude of 183 km as functions of energy. The fluxes have a maximum at 6 eV and then generally decrease with energy. The characteristic photoelectron peak [*Schunk and Nagy*, 2009] appears near 25 eV and is due to ionization by solar EUV photons from the solar HeII 30.4 nm line. The fall-off of flux near 60 eV is due to a fall-off of the solar irradiance with increasing energy as well as a decreasing cross section. The Auger peaks are evident at higher energies (e.g., oxygen peak at 500 eV).

Figure 2a also shows that photoelectron fluxes for energies less than ≈ 10 eV are affected by the thermal electron density as well as by the solar flux, whereas higher energy electrons are not. The photoelectron energy lost to thermal electrons via Coulomb collisions appears as heat for the thermal electron gas. Future work should include appropriate ionospheric densities.

Figure 2b shows upward and downward fluxes at 25 eV versus altitude for the case with normal conditions (blue line in Figure 2a). Below about 200 km the up and down fluxes are the same, and at least at this energy electron transport is not important. That is, the photoelectrons are "local." Given an elastic cross section of 10^{-15} cm^2 [*Gan et al*., 1990, and references therein] and a density of 10^8 cm^{-3}, the mean free path is ≈ 100 km, but the corresponding altitude interval is only ≈ 25 km given the average pitch angle and field draping. Above 200 km photoelectrons can be transported and contribute to an electron escape flux. Note that for closed crustal magnetic field lines the upward electrons would reenter the ionosphere as a down flux [*Liemohn et al*., 2006], but we do not consider this case in our paper.

Figure 3a shows a comparison of our model fluxes with SWEA fluxes for case 1 (1 April 2015). The agreement is reasonable overall, but the higher model flux for $E \approx 25$ eV suggests that the HESSR solar irradiance for $\lambda \approx 30$ nm could be high on this date.

Next we consider the subcases shown in Figure 2. First, the effect of enhancing the short wavelength photon irradiance is obvious—the photoelectron flux is also enhanced, but the effect extends somewhat to lower energies due to cascading. The flux of Auger electrons above 250 eV was especially related to the solar irradiance at 1–2 nm. Similarly, if we had increased the solar irradiance just near $\lambda \approx 30$ nm, then the 25 eV photoelectrons would have had an enhanced flux. The photoelectron fluxes near energies of 10 eV and below

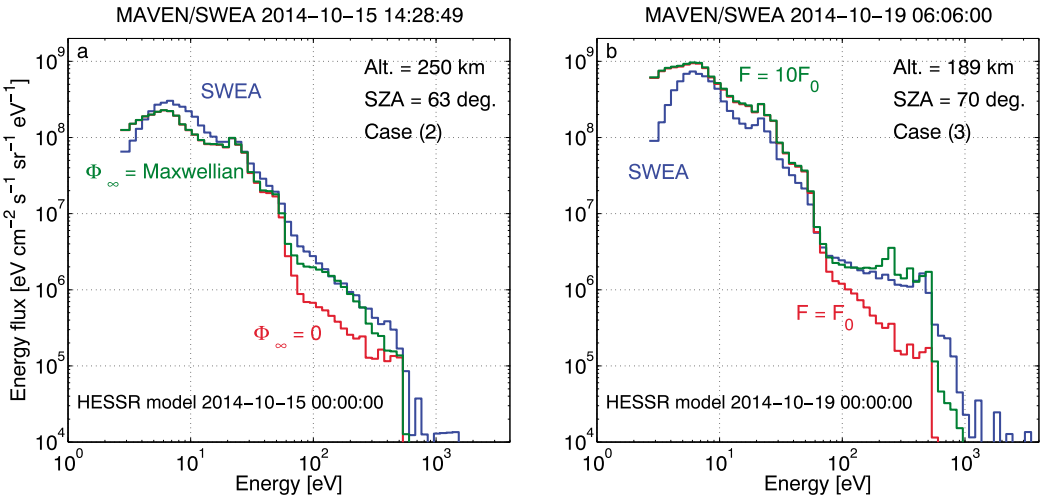

Figure 4. Two-stream model and SWEA energy flux spectra. Blue lines show the SWEA spectrum. (a) 15 October 2014 conditions and external electrons, Φ_∞, are included in the model (see text). (b) 19 October 2014 (a solar flare day) conditions and model results with (red) and without (green) enhanced soft X-ray fluxes ($\lambda < 5$ nm), F_0, are shown. Also note that a CME encountered Mars on this day, but the effects were not included in this model.

depend on the primary production rate at these energies, on cascading production rates, and on losses associated with nonionizing inelastic collisions. In particular, vibrational excitation of CO_2 is important. But electron-electron Coulomb collisions are also important and depend on the thermal electron density, as is evident in Figure 2. Increasing the electron density clearly alters the low-energy flux. Coulomb collisions generate heating of the thermal electrons and lead to enhanced electron temperatures [cf. *Schunk and Nagy*, 2009; *Fox et al*., 2008; *Chen et al*., 1978].

Figure 3b shows model-SWEA comparisons on 3 March 2015 for which the solar zenith angle was 72°. A possible explanation for the better agreement on this date than the other date between SWEA data and model output could be that the assumed HESSR irradiance and thermal electron densities are more accurate for this date.

Case 2. Figure 4a shows the model (red and green) and SWEA (blue) energy fluxes of suprathermal electrons on 15 October 2014. Model runs with and without an external electron flux from the magnetosheath (or tail) were carried out. Clearly, inclusion of external electrons makes a difference for electron energies greater than 100 eV. However, similar results could have been obtained using an enhanced solar soft X-ray irradiance, although there was no evidence for such a flare on this date.

Case 3. Unlike 15 October, a flare was observed on 19 October 2014 and the EUVM instrument on MAVEN detected soft X-ray irradiances 10 times greater than the preceding nonflare times. Figure 4b shows model-SWEA comparisons for this date. HESSR solar irradiance does not include flares, and the associated model electron fluxes are clearly less than the SWEA fluxes above 100 eV. However, the model agrees much better with data when the solar irradiance for λ shortward of 5 nm was enhanced in line with the flare-enhanced solar soft X-ray irradiance measured by the MAVEN EUVM instrument. Enhanced electron fluxes associated with the CME were not included in this model.

5. Summary

We investigated suprathermal electrons in the Martian ionosphere using model comparisons with MAVEN SWEA data. These electrons are important for heating, ionization, and airglow production. Auger processes were included in our code. The paper demonstrated that Auger electron fluxes are a good indicator of the soft X-ray irradiance at Mars, just as the electron flux at 25 eV is a good indicator of the solar EUV irradiance. We predict that the flux of Auger electrons at 250–500 eV is quantitatively related to the solar irradiance at 1–2 nm. We showed that the photoelectron flux for energies less than 10 eV depends on the ionosphere's electron to neutral density ratio. And we also showed that external electron and solar soft X-ray irradiance

inputs can make a significant contribution to the high-energy suprathermal electron flux in the ionosphere, depending on the magnetic topology. We expect that as more MAVEN data become available, we will be able to further refine our understanding of the complex processes involved in the conversion of solar EUV and XUV irradiances to thermal energy in the Martian ionosphere and thermosphere.

Acknowledgments
All data shown in the figures can be obtained from the corresponding author. MAVEN data are in the Planetary Data System. This work was supported by NASA grant NNH10CC04C to the University of Colorado and by subcontract to the University of Kansas. The MAVEN project is supported by NASA through the Mars Exploration Program. This work was also partially supported by CNES for the part based on observations with the SWEA instrument on board MAVEN.

The Editor thanks two anonymous reviewers for their assistance in evaluating this paper.

References

Banks, P. M., and A. F. Nagy (1970), Concerning the influence of elastic scattering upon photoelectron transport and escape, *J. Geophys. Res.*, *75*, 1902–1910, doi:10.1029/JA075i010p01902.

Bougher, S. W. (2012), Coupled MGCM-MTGCM Mars thermosphere simulations and resulting data products in support of the MAVEN mission, JPL/CDP report, pp. 1–9, 6 Aug.

Bougher, S. W., A. Valeille, M. R. Combi, and V. Tenishev (2009), Solar cycle and seasonal variability of the Martian thermosphere-ionosphere and associated impacts upon atmospheric escape, *SAE Int. J. Aerosp.*, *4*(1), 227–237, doi:10.4271/2009-01-2396.

Bougher, S. W., T. E. Cravens, J. Grebowsky, and J. Luhmann (2014), The aeronomy of Mars: Characterization by MAVEN of the upper atmosphere reservoir that regulates volatile escape, *Space Sci. Rev.*, *182*, doi:10.1007/s11214-014-0053-7.

Chen, R. H., T. E. Cravens, and A. F. Nagy (1978), The Martian ionosphere in light of the Viking observations, *J. Geophys. Res.*, *83*, 3871–3876, doi:10.1029/JA083iA08p03871.

Coates, A. J., et al. (2008), Ionospheric photoelectrons at Venus: Initial observations by ASPERA-4, *Planet. Space Sci.*, *56*, 802–806, doi:10.1016/j.pss.2007.12.008.

Coates, A. J., S. M. E. Tsang, A. Wellbrock, R. A. Frahm, J. D. Winningham, S. Barabash, R. Lundin, D. T. Young, and F. J. Crary (2011), Ionospheric photoelectrons: Comparing Venus, Earth, Mars and Titan, *Planet. Space Sci.*, *59*, 1019–1027, doi:10.1016/j.pss.2010.07.016.

Cravens, T. E., and A. N. Maurellis (2001), X-ray emission from scattering and fluorescence of solar X-rays at Venus and Mars, *Geophys. Res. Lett.*, *28*, 3043–3046, doi:10.1029/2001GL013021.

Crider, D. H., D. A. Brain, M. H. Acuña, D. Vignes, C. Mazelle, and C. Bertucci (2004), Mars Global Surveyor observations of solar wind magnetic field draping around Mars, *Space Sci. Rev.*, *111*, 203–221, doi:10.1023/B:SPAC.0000032714.66124.4e.

Dennerl, K. (2002), Discovery of X-rays from Mars with Chandra, *Astron. Astrophys.*, *394*, 1119–1128, doi:10.1051/0004-6361:20021116.

Fontenla, J. M., J. Harder, W. Livingston, M. Snow, and T. Woods (2011), High-resolution solar spectral irradiance from extreme ultraviolet to far infrared, *J. Geophys. Res.*, *116*, D20108, doi:10.1029/2011JD016032.

Fox, J. L., M. I. Galand, and R. E. Johnson (2008), Energy deposition in planetary atmospheres by charged particles and solar photons, *Space Sci. Rev.*, *139*, 1–4, doi:10.1007/s11214-008-9403-7.

Gan, L., T. E. Cravens, and M. Horanyi (1990), Electrons in the ionopause boundary layer of Venus, *J. Geophys. Res.*, *95*, 19,023–19,035, doi:10.1029/JA095iA11p19023.

Gan, L., C. N. Keller, and T. E. Cravens (1992), Electrons in the ionosphere of Titan, *J. Geophys. Res.*, *97*, 12,137–12,151, doi:10.1029/92JA00300.

Lee, J. S., J. P. Doering, T. A. Potemra, and L. H. Brace (1980), Measurements of the ambient photoelectron spectrum from Atmosphere Explorer: I. AE-E measurements below 300 km during solar minimum conditions, *Planet. Space Sci.*, *28*, 947–971, doi:10.1016/0032-0633(80)90058-6.

Liemohn, M. W., et al. (2006), Numerical interpretation of high-altitude photoelectron observations, *Icarus*, *182*, 383–395, doi:10.1016/j.icarus.2005.10.036.

Mahaffy, P. R., M. Benna, M. Elrod, R. V. Yelle, S. W. Bougher, S. W. Stone, and B. M. Jakosky (2015), Structure and composition of the neutral upper atmosphere of Mars from the MAVEN NGMIS investigation, *Geophys. Res. Lett.*, *42*, doi:10.1002/2015GL065329, in press.

Mantas, G. P., and W. B. Hanson (1979), Photoelectron fluxes in the Martian ionosphere, *J. Geophys. Res.*, *84*, 369–385, doi:10.1029/JA084iA02p00369.

Mitchell, D. L., R. P. Lin, H. Rème, D. H. Crider, P. A. Cloutier, J. E. P. Connerney, M. H. Acuña, and N. F. Ness (2000), Oxygen Auger electrons observed in Mars' ionosphere, *Geophys. Res. Lett.*, *27*, 1871–1874, doi:10.1029/1999GL010754.

Nagy, A. F., and P. M. Banks (1970), Photoelectron fluxes in the ionosphere, *J. Geophys. Res.*, *75*, 6260–6270, doi:10.1029/JA075i031p06260.

Ozak, N., T. E. Cravens, G. H. Jones, A. J. Coates, and I. P. Robertson (2012), Modeling of electron fluxes in the Enceladus plume, *J. Geophys. Res.*, *117*, A06220, doi:10.1029/2011JA017497.

Richard, M. S., T. E. Cravens, I. P. Robertson, J. H. Waite, J.-E. Wahlund, F. J. Crary, and A. J. Coates (2011), Energetics of Titan's ionosphere: Model comparisons with Cassini data, *J. Geophys. Res.*, *116*, A09310, doi:10.1029/2011JA016603.

Schunk, R. W., and A. F. Nagy (2009), *Ionospheres: Physics, Plasma Physics, and Chemistry*, 2nd ed., Cambridge Univ. Press, Cambridge, U. K.

Shutte, N. M., et al. (1989), Observation of electron and ion fluxes in the vicinity of Mars with the HARP spectrometer, *Nature*, *314*, 614–616, doi:10.1038/341614a0.

Víkor, G., A. Hiltunen, S. Ricz, B. Sulik, and Á. Kövér (1998), The O and C K-VV Auger-electron spectra from CO_2 molecule induced by 1.0 MeV photon impact, Annual report 1997 in Institute of Nuclear Research of the Hungarian Academy of Sciences, pp. 31–32, EP Systema BT, Debrecen, Hungary.

Erratum

In the originally published version of this article, Figure 3b mistakenly displayed electron energy fluxes for 19 October 2014 instead of the correct date of 3 March 2015. Figure 3b has since been updated with the electron energy fluxes for 3 March 2015. The new corrected model electron flux is about 20% less than the original flux near an energy of 30 eV and about 50% lower at 400 eV, which is not enough to change the conclusions. This version may be considered the authoritative version of record.